

See discussions, stats, and author profiles for this publication at: <https://www.researchgate.net/publication/235668197>

Optical, Structural, and Numerical Investigations of GaAs/AlGaAs Core–Multishell Nanowire Quantum Well Tubes

ARTICLE in NANO LETTERS · FEBRUARY 2013

Impact Factor: 13.59 · DOI: 10.1021/nl304182j · Source: PubMed

CITATIONS

32

READS

90

13 AUTHORS, INCLUDING:



Melodie A Fickenscher

University of Cincinnati

30 PUBLICATIONS 405 CITATIONS

[SEE PROFILE](#)



Howard E. Jackson

University of Cincinnati

325 PUBLICATIONS 3,523 CITATIONS

[SEE PROFILE](#)



Bryan M. Wong

University of California, Riverside

89 PUBLICATIONS 1,457 CITATIONS

[SEE PROFILE](#)



Chennupati Jagadish

Australian National University

282 PUBLICATIONS 3,469 CITATIONS

[SEE PROFILE](#)

Optical, Structural, and Numerical Investigations of GaAs/AlGaAs Core–Multishell Nanowire Quantum Well Tubes

Melodie Fickenscher, Teng Shi, Howard E. Jackson, and Leigh M. Smith*

Department of Physics, University of Cincinnati, Cincinnati, Ohio 45221-0011, United States

Jan M. Yarrison-Rice

Department of Physics, Miami University, Oxford, Ohio 45056, United States

Changlin Zheng, Peter Miller, and Joanne Etheridge

Monash Centre for Electron Microscopy, Monash University, Victoria, 3800 Australia

Bryan M. Wong

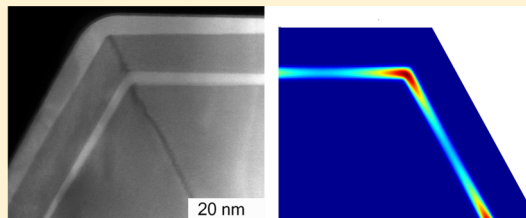
Sandia National Laboratories, Livermore, California 94551, United States

Qiang Gao, Shriniwas Deshpande, Hark Hoe Tan, and Chennupati Jagadish

Department of Electronic Materials Engineering, Research School of Physics and Engineering, The Australian National University, Canberra, ACT 0200, Australia

Supporting Information

ABSTRACT: The electronic properties of thin, nanometer scale GaAs quantum well tubes embedded inside the AlGaAs shell of a GaAs core–multishell nanowire are investigated using optical spectroscopies. Using numerical simulations to model cylindrically and hexagonally symmetric systems, we correlate these electronic properties with structural characterization by aberration-corrected scanning transmission electron microscopy of nanowire cross sections. These tubular quantum wells exhibit extremely high quantum efficiency and intense emission for extremely low submicrowatt excitation powers in both photoluminescence and photoluminescence excitation measurements. Numerical calculations of the confined eigenstates suggest that the electrons and holes in their ground states are confined to extremely localized one-dimensional filaments at the corners of the hexagonal structure which extend along the length of the nanowire.



KEYWORDS: Nanowire, quantum confinement, excitation spectroscopy, modeling

A significant advantage to vapor–liquid–solid (VLS) growth of semiconductor nanowires is the capability to fabricate complex core–multishell heterostructures of different materials. For example, recently core–multishell heterostructures have been investigated for tunable nitride nanowire (NW) lasers¹ or type-II InP/InAs structures.² However, the quantum effects in these NW heterostructures are frequently masked by the strong strain or piezoelectric effects present in these strained-layer materials which can affect both the confinement potentials as well as the band structure.^{3,4} In this Letter, we introduce a new form of a strain-free semiconductor nanowire heterostructure with unique properties including quantum confined states that are sensitive to the hexagonal growth facets of the nanowire heterostructure. We have grown high-quality GaAs/AlGaAs

core–multishell structures where the electronic states are quantum confined to a very thin shell surrounding the semiconductor core, and all layers are essentially strain-free. Here we present data for two samples, one with a quantum well tube (QWT) thickness of nominally 8 nm and one with a QWT thickness of nominally 4 nm. Because the states are quantum confined in two dimensions, but free particles along the axis of the nanowire, the electrons and holes confined to the QWTs are truly one-dimensional.

Received: November 12, 2012

Revised: February 2, 2013

Published: February 19, 2013

We show in this Letter that the observed optical properties of the ground and excited states are consistent with the structure of the core–multishell nanowire as determined by aberration-corrected high-angle annular dark field (HAADF) scanning transmission electron microscopy (STEM) and calculations using a simple eigenfunction expansion for a cylindrically symmetric model system as well as a more complex finite-element calculation that calculates the confined eigenstates that reflect the faceted, that is hexagonally symmetric, core–multishell nanowire. These more complex calculations show that the electrons and holes are strongly confined to the corners of the QWT resulting in filaments along the axis of the nanowire. Such new structures suggest the versatility of semiconductor nanowire heterostructures has not yet reached its limit. In what follows we discuss the nanowire heterostructure growth, provide STEM and energy dispersive X-ray spectroscopy (EDX) evidence of the core/multishell structure and composition, present photoluminescence and photoluminescence excitation data and then interpret this data with the aid of two theoretical models.

Nanowire Core/Multishell Growth. The radial quantum well nanowires were grown using metalorganic chemical vapor deposition (MOCVD) with 50 nm Au nanoparticles as catalyst. The GaAs core was grown using 50 nm Au catalyst and a two-temperature growth procedure developed by Joyce et al.⁵ GaAs nanowires grown by this two-temperature procedure have been shown to be twin-defect free with little tapering and have long carrier lifetimes.⁶ Following the core growth, a 90 nm AlGaAs shell was grown at 650 °C with nominally 66% Al in vapor. After the first AlGaAs shell, a thin GaAs shell was grown to serve as the QW. Nanowire samples with nominal QW widths of 4 and 8 nm QW were grown by adjusting the growth time. After the GaAs QW, a second 25 nm AlGaAs shell was grown and capped by a 10 nm GaAs shell to prevent oxidation of the AlGaAs.

The resultant structures were characterized by cross sectional and plan-view high-resolution TEM and cross-sectional HAADF-STEM and EDX to determine the size and structure of the QWT as well as measure the Al concentration of the shell. Plan-view TEM images (not shown here) show nanowires that are only slightly tapered along the axis of the NW with lengths of ~4 μm. In Figure 1, we show HAADF-STEM images

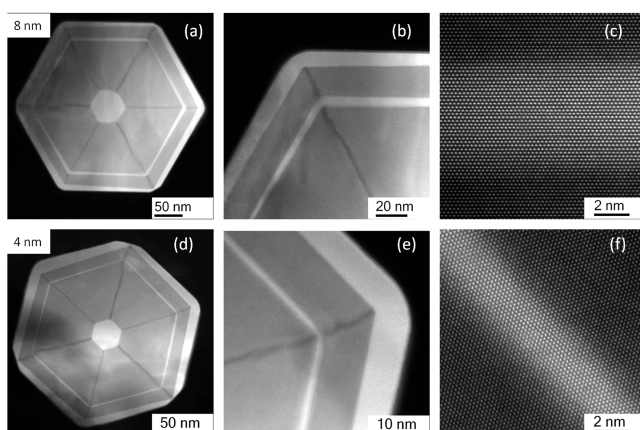


Figure 1. Cross-sectional HAADF STEM images from the nominally 8 nm (a–c) and 4 nm (panels d–f) QWT NW samples shown at several magnifications. Note the approximate hexagonal facets and the crystal quality.

at three different magnifications of microtomed cross sections of the NW that were obtained on an FEI Titan³ 80–300 Schottky field emission gun TEM/STEM fitted with spherical aberration-correctors (CEOS GmbH) on the probe and image-forming lenses and operating at 300 kV. The intensity of HAADF-STEM images is proportional to Z^n where Z is the atomic number (Z) of the constituent atoms and n depends in a complicated way on the experimental conditions but is typically $1 < n < 2$.^{7,8} Regions of high intensity correspond to the GaAs, while those of lower intensity correspond to AlGaAs and this was confirmed by EDX. For the nominal 8 nm sample, for instance, a light 50 nm GaAs core at the center is readily visible, and is followed by a 90 nm AlGaAs shell, after which a thin GaAs quantum well of a few nanometers is shown by the thin light band. The second AlGaAs shell (~25 nm thick) that forms the outer barrier wall of the quantum well is also seen along with the final 10 nm GaAs capping layer. A quantitative analysis of the EDX spectra determined the aluminum concentration, x, in $\text{Al}_x\text{Ga}_{1-x}\text{As}$ to be 0.5 ± 0.1 . The QW is parallel to the {110} planes while the corners of the well lie parallel to the {112} facets.

In Figure 2a–c, the image intensity varies across the width of the GaAs QWT suggesting a variation in composition across the well. It is reasonable to assume that the central maximum corresponds to GaAs and minimum corresponds to $\text{Al}_x\text{Ga}_{1-x}\text{As}$ (where $x = 0.5 \pm 0.1$) and that $x < 0.5$ between the minimum and maximum. Detailed HAADF-STEM images of the three corners corresponding to the thickest parts of the QW in the nominal 8 nm sample (Figure 2a) show that the midpoint (M) is typically the widest part of the well, and that one side (R) is wider than the other (L). The histograms in Figure 2d show L, R, and M widths determined from 15 images (3 “thick” corners of 5 cross sections) (see Figure 2b) and that correspond approximately to the full width at 20% of the maximum determined from linescans (Figure 2c). Widths determined from fwhm of the linescans are about 15% narrower. These histograms provide some measure of the wire-to-wire variation of the QW widths. A similar analysis of the nominal 4 nm sample gives a QW width of approximately 3 nm.

In each case, the QWT is continuous around the circumference of the NW. The cross-sectional HAADF-STEM images show narrow aluminum rich (dark) regions along the diagonals of the side facets (and this was confirmed by EDX). The Al rich region does not cross the QW region. These narrow Al rich regions reflect a self-ordering that is seen in both epitaxial⁹ and nanowire growth of alloys.^{10,11} The mechanism of this segregation is theorized to be the differences in the diffusion rate of the Ga and Al adatoms during the growth process.¹⁰

Single Nanowire Photoluminescence. To obtain optical data on individual nanowire heterostructures, the nanowires were transferred mechanically from the growth substrate to a marked silicon substrate. Low-temperature (10 K) micro-photoluminescence (micro-PL) spectra of single nanowires were acquired by mounting the silicon substrate to the coldfinger of a constant-flow liquid helium microcryostat and using 532 nm CW or 742 nm pulsed/CW laser excitation. Single nanowires were imaged using a long working length 50× objective that also focused the excitation laser to a 1.5 μm spot. The PL emitted from the single nanowire was imaged onto the entrance slit of a 250 mm focal length spectrometer and a back-illuminated cooled charge-coupled device (CCD) was used as a detector.

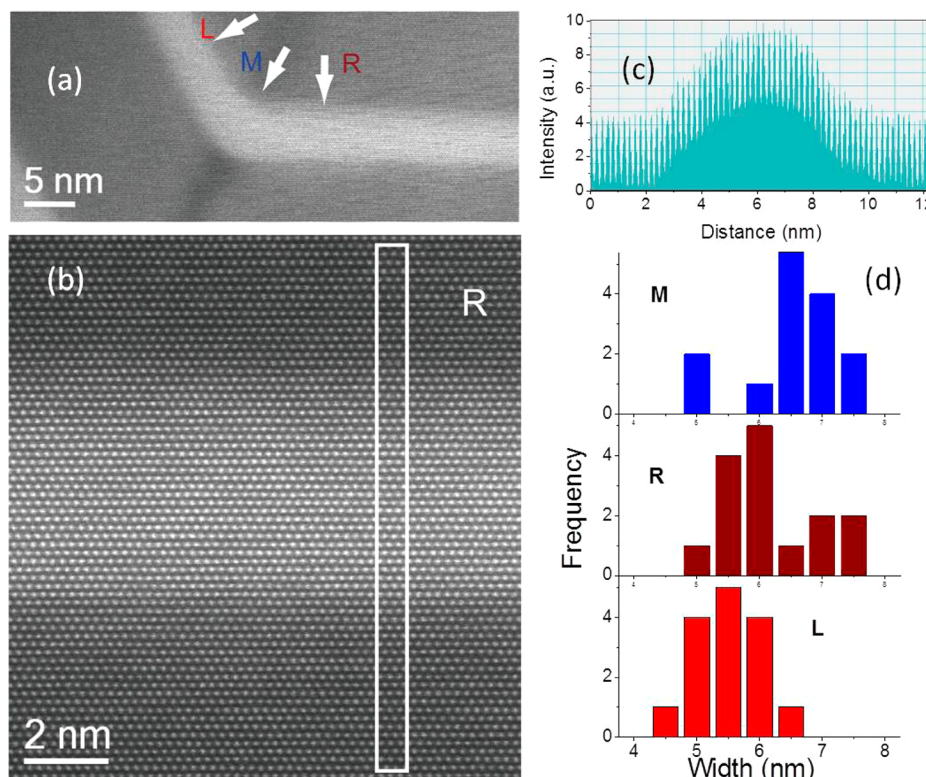


Figure 2. (a) Aberration-corrected HAADF-STEM image of a representative cross section of the nominally 8 nm QWT NW. L, M, and R show placement of widths determined near the corners of the QWT. (b) Higher-resolution image taken near L in (a). (c) An intensity line-scan taken across the image shown in (b). (d) Histogram showing L, M, and R widths of three corners from five cross sections of nanowires (15 total measurements).

The photoluminescence spectra displayed in Figure 3 provide strong evidence for quantum confinement provided

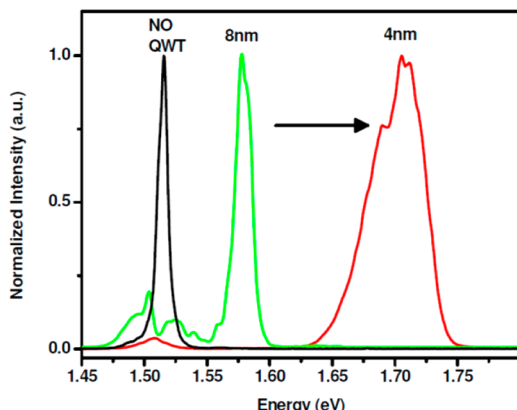


Figure 3. Black solid line shows PL emission from a representative single GaAs/AlGaAs core–shell nanowire. Green and red solid lines show PL emission from a single nominal 8 nm and nominal 4 nm QWT NW. The integrated intensities for the QWT samples are typically 3 orders of magnitude larger than for standard GaAs/AlGaAs core–shell nanowires.

by the GaAs QWT. The PL shows very high quantum efficiency with strong emission for even submicrowatt laser power excitation. The PL response of a GaAs/AlGaAs nanowire without the QWT shows only a response from the GaAs core, as expected. The PL from the GaAs core is seen in all three samples, but intense peaks at higher energy dominate the NW emission for the 4 nm and 8 nm QWT nanowires. The 8 nm

QWT nanowire shows an intense emission at 1.58 meV, which is 60 meV higher in energy than the core emission, while the 4 nm QWT nanowire shows a broader peak at 1.7 eV, nearly 200 meV higher in energy than the GaAs core emission. The integrated intensities from both the 8 and 4 nm QWT nanowires are typically 3 orders of magnitude stronger than that for optimal GaAs/AlGaAs nanowires.⁶ As we shall see, these intense emission bands are consistent with ground state emission for electrons and holes, that is the E₁ to HH₁ transition energy, confined to the respective QWTs.

Two Theoretical Models. To understand the emission from the QWT nanowires, the confined electron and hole eigenstates were calculated using two methods. The first used an eigenfunction expansion method that provides a rapid and easy means for estimating the confinement energies and wave functions for these nanowires. In this method, the confinement potentials from the hexagonally symmetric wire were approximated as being cylindrically symmetric with a 25 nm radius GaAs core, a 90 nm AlGaAs shell, varying QWT thicknesses, and an outer 25 nm AlGaAs shell. The confined states in such a nanowire are determined by three quantum numbers only: the principal quantum number that describes the number of radial nodes, a quantum number that determines the orbital angular momentum (in units of $\hbar/2\pi$) for electrons and holes circulating around the z-axis, and the momentum of the electrons and holes that are free to move along the z-direction (the long direction of the nanowire). We expect that the lowest energy optically active states will be the zero orbital angular momentum states, and so we expand states confined to the QWT potential to be linear expansions over 50 or more cylindrically symmetric eigenstates confined to a cylindrically

symmetric wire with infinite potentials determined by the outer edge of the outer AlGaAs shell. Solutions are easily obtained by inversion of the resulting 2500×2500 matrix that determines the confinement energies and wave functions of the electrons and holes confined to the QWT potential. Electron and hole masses and dielectric constants for GaAs were taken from tabulated values in the literature.

Results for these zero orbital angular momentum states are shown in Figure 4 as a function of QWT thickness for AlGaAs

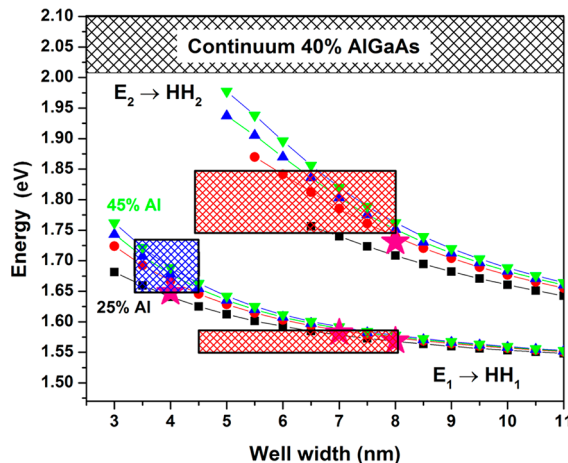


Figure 4. Symbols connected by lines shows results of the cylindrically symmetric eigenfunction expansion model for the $n = 1$ and $n = 2$ eigenstates for Al concentrations of 25% (■), 35% (●), 40% (▲) and 45% (▼). Stars (★) show the results of the hexagonally symmetric finite element calculation for 4, 7, and 8 nm QW widths embedded within 40% AlGaAs barriers. Red-filled rectangles show range of well widths and PL and PLE linewidths derived from Figures 1, 2, 3, and 9. Blue filled rectangle shows equivalent results from the 4 nm QWT sample.

alloy concentrations of 25% (squares), 35% (circles), 40% (up triangles) and 45% (down triangles). The $|E_1, HH_1\rangle$ exciton energies in Figure 4 are calculated as ground state electron (E_1) and heavy hole (HH_1) energies added to the GaAs band edge energy. The widths of the lower red and blue hashed boxes show the range of values for the QWT widths extracted from

HAADF-STEM images (e.g., Figure 2d), while the heights of these boxes show the fwhm range of the photoluminescence from the 4 and 8 nm QWT NWs. The cylindrically symmetric calculations provide a rapid means of estimating the confined states for a particular structure. However, from these calculations we might conclude that the 8 nm QWT NW emits mainly from a somewhat larger than 8 nm QWT, which would be significantly wider than the histogram in Figure 2d from HAADF-STEM images. Similarly, the emission band from the 4 nm QWT NW is consistent with a 4 nm QWT width, but this is also wider than that determined from the HAADF-STEM images.. Expected energies for the $|E_2, HH_2\rangle$ exciton excited states are also shown in Figure 4. From this we conclude that the 8 nm QWT should possess two confined states, while in the 4 nm QWT NW only a single ground state is expected. We will explore this possibility with photoluminescence excitation spectroscopy after considering a second, hexagonally symmetric theoretical model.

While the cylindrical eigenfunction calculation provides a good reference point for these structures, it is clear that it does not completely accurately describe the confined states in these materials since the emission energy of the two nanowires shown here are consistent with wider well widths than expected from the HAADF-STEM structural analysis. To provide more guidance on the eigenstate energies and wave functions, we have used finite element calculations that reflect the actual hexagonally symmetric potential profiles of these nanowires.

To numerically implement the solution of the Schrödinger equation for both the electrons and holes within a proper hexagonally symmetric multicore shell nanowire geometry, we modified a customized finite element code described further in Wong et al.¹² The QWT was modeled as a uniform thickness (no tapering or Al concentration gradients) well wrapped around a 25 nm wire and 90 nm AlGaAs shell. Effective electron/hole masses and band offsets were chosen based on an $x = 0.40$ Al concentration. For each calculation, we used a very dense grid consisting of 200 000 triangular elements that we found necessary to accurately describe the highly localized and oscillatory wave functions within the GaAs quantum well. The solution of the Schrödinger equation was expanded in the basis of the triangular mesh points, yielding a sparse eigenvalue

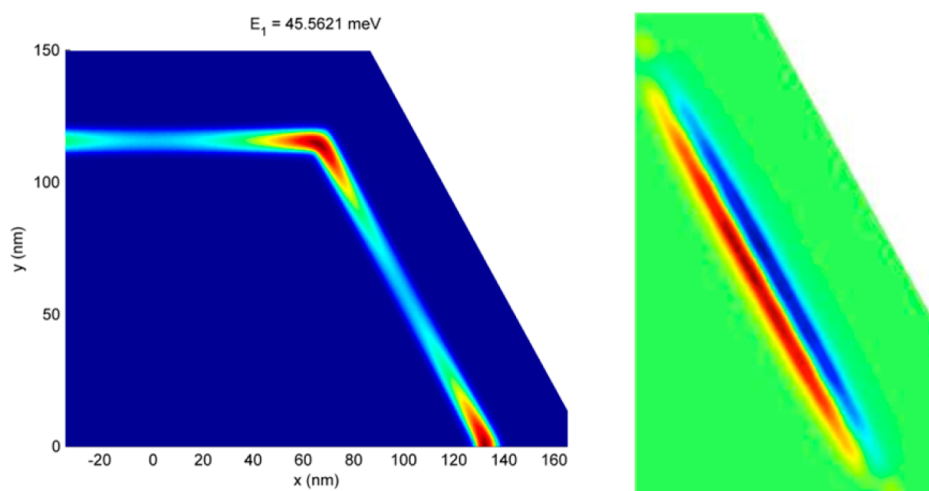


Figure 5. (a) False-color image of the ground state ($E_1 = 45.6$ meV) for the electrons in the 8 nm QWT as calculated by the finite element calculation as described in the text. (b) Image of the excited state ($E_2 = 182$ meV) for the electrons.

equation which is solved iteratively to obtain both the eigenenergies and envelope wave functions.

Upon convergence, the calculation shows the remarkable result that the ground states for all electron and hole states are strongly localized to the corners of the QWT. In Figure 4 above, the sum of the electron and hole confinement energies are used to show the position of the ground $n = 1$ states for QWT of thickness 8, 7, and 4 nm by the red stars. At each thickness, the ground state is seen to be slightly below the calculated ground state energies determined from the cylindrical model. The reason becomes clear in Figure 5a where we show that the electron E_1 ground state wave function for the 8 nm QWT. Remarkably, the corner-localized ground states exhibit true one-dimensional quantum wirelike confined states that should be localized along each corner, running along the length of the wire for perfectly uniform QWTs. The energy is a bit lower than the equivalent cylindrically symmetric calculation because of this confinement to the wider corners. Unexpectedly, the $n = 2$ electron states (see Figure 5b) are predominantly confined to the long facets of the QWT probably as a result of the very high energy cost to create the extra radial node. The 4 nm calculation results in a E_1 wave function (see Figure 6) which is even more tightly confined to

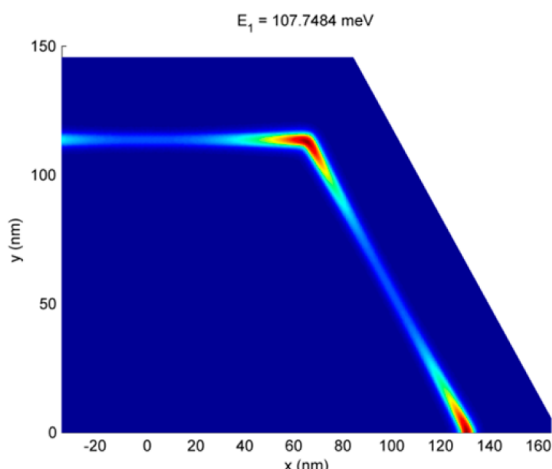


Figure 6. False-color image of the ground state ($E_1 = 107.7$ meV) for the electrons in the 4 nm QWT as calculated by the finite element calculation as described in the text.

the corners than the 8 nm well. No electron or light hole excited states are found for the 4 nm QWT, but there are several heavy hole confined states. Similar corner-confined electron and hole states were observed recently in X-ray microscopy of the PL emitted from a InGaN ~ 800 nm diameter QWT.¹³

In the above analysis, the calculations were limited to wave functions that do not show angular nodes around the QWT. However, these are not the only states possible. In the cylindrical model, orbital angular momentum about the nanowire axis is a good quantum number. The lowest energy states for each radial mode have zero orbital angular momentum. These states are expected to be optically active, but one should also expect a large number of higher order orbital angular momentum states that would show angular nodes along the circumference of the QWT. Many of these states are not localized to the corners of the structure but they show strong effects from the hexagonal symmetry (see

Supporting Information). The energies expected for these higher states should vary as $L^2/2mR^2 = m^2\hbar^2/8\pi^2m^*R^2$ where $L = mh/2\pi$ is the orbital angular momentum (quantized in units of $\hbar/2\pi$), m^* is the effective mass of the electron or hole, and R is the radius of the QWT. The parabolic behavior of these higher lying states are shown as red squares (for the $n = 1$ radial states) and red circles (for $n = 2$ radial states) for an 8 nm QWT in Figure 7. These higher order states are closely separated in energy for small orbital angular momenta but become more separated at higher energies.

While the angular momentum is not expected to be a good quantum number for the hexagonally symmetric solutions, it is reasonable to expect that the solutions exhibit some correspondence with the cylindrically symmetric model. In particular, while the lowest energy radial modes should not exhibit angular nodes, there should be a sequence of states at higher energies where more and more angular nodes appear, until the next radial mode occurs. For comparison, the quantum well states extracted from the finite element solutions are separated between $n = 1$ and $n = 2$ radial solutions and ordered by energy. These states are plotted as blue squares for $n = 1$ and blue circles for the $n = 2$ radial states in Figure 7. The lowest energy $n = 1$ states are confined to the corners of the quantum well as described before, while the lowest lying $n = 2$ states are confined along the facets. For the $n = 1$ radial states, over 100 states that exhibit increasing number of angular nodes extend to higher energy before the $n = 2$ radial states occur. Examples of the wave functions calculated in the hexagonal model with large numbers of angular nodes for the $n = 1$ and $n = 2$ states are shown to the right of Figure 7.

For both the cylindrical and hexagonal models such structure results in a significantly higher density of electron states near the bottom of the $n = 1$ and $n = 2$ radial states. These density of states are shown as histograms of the number of quantum states per 3 meV energy interval in Figure 8. There is a close correspondence between the cylindrical and hexagonal models that show a narrow peak at low energy for the $n = 1$ radial states, and a somewhat broader peak for the $n = 2$ radial states. This sharp buildup of states near the lowest energies of the $n = 1$ and $n = 2$ radial modes will become even more prominent if one includes the free particle behavior along the z -axis (the length of the nanowire) which exhibits the standard $1/E$ density of states for one-dimensional motion. Many of these closely lying electronic states with higher angular momentum exhibit probabilities along the facets rather than the corners. More details on how the wave functions of these closely lying states are affected by the hexagonal nature of the confinement potential are shown in the Supporting Information. As noted previously the energy spacing of these nonzero orbital angular momentum states varies as $L^2/2mR^2$. As the radius of the QWT is reduced, the energy spacing of these states is significantly increased so that nearly perfect one-dimensional confinement to the corners might be obtained.

By comparing the hexagonal calculations with the cylindrical model and the measured PL spectra, we conclude that the hexagonal model should work well for well widths of 3 nm for the nominally 4 nm QWT, which is consistent with the HAADF-STEM images, and 7 or 8 nm for the nominally 8 nm QWT, which is on the high side of the measured histograms in Figure 2d. In both cases, the hexagonal model suggests that both electrons and holes are strongly confined to the QWT corners. We next return to the excited state behavior by

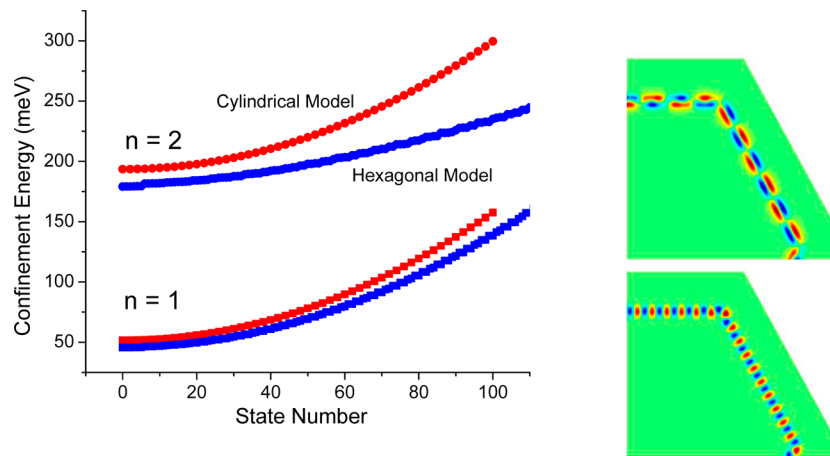


Figure 7. Energy as a function of the state number for angular modes for the $n = 1$ (squares) and $n = 2$ (circles) radial eigenstates as calculated by the cylindrically symmetric eigenfunction expansion (red symbols) and the hexagonally symmetric finite element calculation (blue symbols). Right panel shows representative higher order angular wavefunctions for the $n = 1$ and $n = 2$ radial modes.

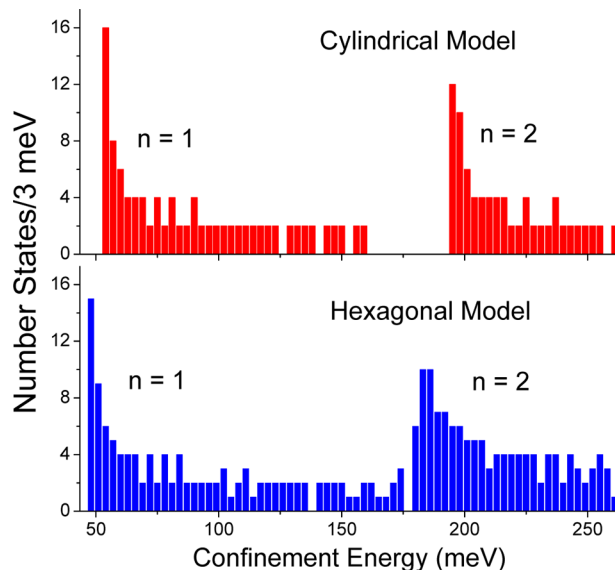


Figure 8. Histogram of the number of eigenstates in 3 meV intervals for the cylindrically symmetric eigenfunction expansion calculation, and the hexagonally symmetric finite element calculation. The increased density of states at the bottom of the $n = 1$ and $n = 2$ radial states is clear in both models.

carrying out photoluminescence excitation (PLE) measurements.

Photoluminescence Excitation Spectroscopy. In order to probe the excited state behavior of these QWTs, we have implemented photoluminescence excitation spectroscopy employing a 200 fs 800 nm pulse from a mode-locked Ti-sapphire laser to create a white light super continuum using a photonic crystal fiber. Using a pulse-shaper, 200 fs laser pulses can be extracted from the supercontinuum with wavelengths between 590 and 1500 nm with a spectral bandwidth of 3 nm. PLE spectra from the nominal 4 and 8 nm QWTs are displayed in Figure 9. The PL emission from single nanowires is also shown as solid lines: black solid line showing emission from the core and red solid lines showing emission from the QWT. PLE spectra associated with the core and QWT emission are shown as red and black symbols. All lines show evidence for excitations into the AlGaAs barrier, which are consistent with a 40%

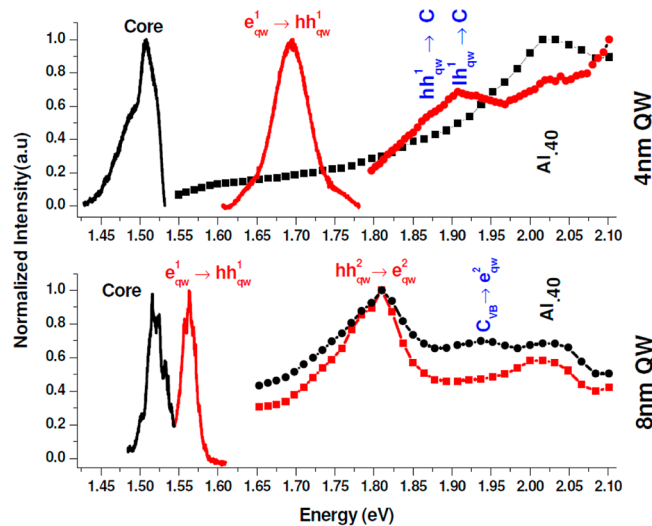


Figure 9. Photoluminescence and photoluminescence excitation measurements for a single nominal (a) 4 nm and (b) 8 nm QWT NW. Black solid lines and symbols show PL and PLE associated with the core states, while red solid lines and symbols show PL and PLE associated with the QWT emission.

AlGaAs concentration. The 8 nm QWT PLE spectrum shows a prominent excitation peak that corresponds to excitations from HH_2 to E_2 and a smaller peak associated with a transition from a hole just above the AlGaAs barrier to the second confined electron state. The prominent HH_2 to E_2 transition corresponds very closely to the expected values from the eigenfunction expansion energies shown in Figure 4 for a QWT with a 6–7 nm width (which would be consistent with the HAADF-STEM results), but such widths are too narrow to match the ground-state energies for the 8 nm width. The fact that the excited state transition is at a higher energy than expected from the ground-state energy may reflect the fact that the QW is significantly tapered with three wider corners and three narrower ones. This would tend to shift the E_2 and HH_2 confined states since they are confined along the flat facets of the QWT (not the corners) and so would be much more sensitive to the tapering of the QWT. The PL emission from the 4 nm QWT is consistent with the 4 nm cylindrically symmetric calculation or a ~3 nm hexagonally symmetric

calculation. As predicted, the 4 nm QWT nanowire shows no evidence for a second confined electron state, but does show a small peak which can be associated with a transition from a confined HH₂ or LH₂ hole to an electron just above the AlGaAs conduction band barrier. (A similar hole to electron continuum peak is also seen in the 8 nm PLE spectrum.)

In the above discussion, we have demonstrated that both PL and PLE spectroscopic results are broadly consistent with both the structural HAADF-STEM images of the QWT NWs as well as both the cylindrically symmetric and the more complex hexagonally symmetric calculations of the wave functions that were selected to show no nodes along the circumference of the QWT.

Summary. In this Letter, we have shown that the optical emission and excitation properties measured for single core-multishell GaAs/AlGaAs QWTs can be understood in terms of numerical calculations of the confined electron and hole states that are guided by atomic-resolution HAADF-STEM imaging of the nanowire cross sections. The fabricated nanowires show extremely high quantum efficiency with significant ground-state emissions observed even for submicrowatt excitation powers. Remarkably, detailed numerical calculations of the electron and hole eigenstates show that the ground states are localized to one-dimensional filaments along the corners of the hexagonally symmetric structure and extend along the length of the nanowire. Indeed, this shows that the wave functions can be sensitively controlled through adjustment of either the well width, radius or the geometry of the QWT.

■ ASSOCIATED CONTENT

Supporting Information

Additional information and figures. This material is available free of charge via the Internet at <http://pubs.acs.org>.

■ AUTHOR INFORMATION

Corresponding Author

*E-mail: leigh.smith@uc.edu.

Notes

The authors declare no competing financial interest.

■ ACKNOWLEDGMENTS

We acknowledge the help of Yanan Guo and Jin Zou of the University of Queensland who prepared the nanowire cross sections. We acknowledge the support of the National Science Foundation through Grants DMR-1105362, 1105121, and ECCS-1100489. B.M.W. was supported by the Solid-State Lighting Science Center, an Energy Frontier Research Center (EFRC) funded by the U.S. Department of Energy, Office of Science, Office of Basic Energy Sciences (BES), and the BES Division of Materials Science and Engineering. Additional support provided by the Laboratory Directed Research and Development program at Sandia National Laboratories, a multiprogram laboratory operated by Sandia Corporation, a Lockheed Martin Company, for the United States Department of Energy under contract DE-AC04-94-AL85000. We also acknowledge the support of the Australian Research Council (ARC). The Australian National Fabrication Facility is acknowledged for access to the growth facilities used in this research. The FEI Titan³ 80-300 S/TEM at Monash Centre for Electron Microscopy was funded by the ARC Grant LE0454166.

■ REFERENCES

- (1) Fang, Q.; Gradecak, S.; Yat, L.; Cheng-Yen, W.; Lieber, C. M. *Nano Lett.* **2005**, *5*, 2287–91.
- (2) Mohan, P.; Motohisa, J.; Fukui, T. *Appl. Phys. Lett.* **2006**, *88*, 133105–1–3.
- (3) Pistol, M. E.; Pryor, C. E. *Phys. Rev. B* **2008**, *78*, 115319–1–12.
- (4) Montazeri, M.; Fickenscher, M.; Smith, L. M.; Jackson, H. E.; Garrison-Rice, J.; Kang, J. H.; Gao, Q.; Tan, H. H.; Jagadish, C.; Guo, Y.; Zou, J.; Pistol, M.; Pryor, C. E. *Nano Lett.* **2010**, *10*, 880–886.
- (5) Joyce, H. J.; Gao, Q.; Tan, H. H.; Jagadish, C.; Kim, Y.; Zhang, X.; Guo, Y. N.; Zou, J. *Nano Lett.* **2007**, *7*, 921–926.
- (6) Perera, S.; Fickenscher, M. A.; Jackson, H. E.; Smith, L. M.; Garrison-Rice, J.; Joyce, H. J.; Gao, Q.; Tan, H. H.; Jagadish, C.; Zhang, X.; Zou, J. *Appl. Phys. Lett.* **2008**, *93*, 053110–3.
- (7) Kirkland, E.; Loane, R.; Silcox, J. *Ultramicroscopy* **1987**, *23*, 77–96.
- (8) Hartel, P.; Rose, H.; Dinges, C. *Ultramicroscopy* **1996**, *63*, 93–114.
- (9) Biasiol, G.; Gustafsson, A.; Leifer, K.; Kapon, E. *Phys. Rev. B* **2002**, *65*, 205306–1.
- (10) Skold, N.; Wagner, J. B.; Karlsson, G.; Hernan, T.; Seifert, W.; Pistol, M. E.; Samuelson, L. *Nano Lett.* **2006**, *6*, 2743–2747.
- (11) Wagner, J. B.; Skold, N.; Wallenberg, L. R.; Samuelson, L. *J. Cryst. Growth* **2010**, *312*, 1755–1760.
- (12) Wong, B. M.; Leonard, F.; Li, Q. M.; Wang, G. T. *Nano Lett.* **2011**, *11*, 3074–3079.
- (13) Martinez-Criado, G.; Homs, A.; Alen, B.; Sans, J. A.; Segura-Ruiz, J.; Molina-Sanchez, A.; Susini, J.; Yoo, J.; Yi, G. *Nano Lett.* **2012**, *12* (11), 5829–5834.